Hybrid density functional study of the structural, bonding, and electronic properties of bismuth vanadate

Kyoung E. Kweon and Gyeong S. Hwang[*]

Department of Chemical Engineering, University of Texas at Austin, Austin, Texas 78712, USA

The structure and property prediction of metal oxides can significantly be improved by incorporating exact Hartree-Fock (HF) exchange into density functional theory (DFT), which is the so-called hybrid DFT. We explored the impact of HF exchange inclusion on the predicted structural, bonding, and electronic properties of bismuth vanadate ($BiVO_4$), with particular attention to the difference between its monoclinic and tetragonal scheelite phases. The applied exchange-correlation (xc) functionals include the gradient corrected Perdew-Burke-Ernzerhof (PBE) and the PBE-HF hybrid functionals with HF exchange amounts of 10%, 25%, and 50%. We find that the PBE-HF25% yields a monoclinic structure in very close agreement with the experimentally determined structure, while the PBE-HF50% tends to overestimate the monoclinic distortion and the PBE/PBE-HF10% can hardly identify a distinct monoclinic configuration at ambient conditions. Electronic structure analysis reveals that the increasing monoclinic distortion with the amount of HF exchange is related to the enhancement of hybridization between Bi $6s$-O $2p$ antibonding states and unoccupied Bi $6p$ states. The bonding mechanisms and band structures of the monoclinic and tetragonal phases of $BiVO_4$ were also investigated, and we discuss how the predictions are sensitive to the xc functional choice.

PACS number(s): 71.15.Mb, 71.20.Nr, 61.50.−f

I. INTRODUCTION

Metal-oxide semiconductors have been recognized as promising photocatalysts for water splitting by virtue of their low production cost and high stability in aqueous environments.[1,2] Previous studies mostly focused on binary metal oxides such as TiO_2, Fe_2O_3, and WO_3; they show reasonable photocatalytic performance, but also have some inherent limitations.[2,3] For example, TiO_2 has been most widely used due to its strong photoinduced redox power, high photocorrosion resistance, and nontoxicity; however, due to its large band gap (≈ 3 eV) the photocatalytic activity of TiO_2 is largely limited to UV radiation.[4,5] During recent years, much attention has been turned to multicomponent metal oxides to expand the search for better visible-light-active photocatalysts.

Bismuth vanadate ($BiVO_4$) has recently emerged as a viable candidate for photocatalytic water oxidation.[1,6–12] $BiVO_4$ mainly exists in three different crystal phases such as tetragonal zircon (tz-), tetragonal scheelite (ts-), and monoclinic scheelite (ms-).[13] Among them, ms-$BiVO_4$ exhibits the highest photocatalytic activity under visible light irradiation.[11,12] The lower activity of tz-$BiVO_4$ has been explained by the relatively large band gap of 2.9 eV, while ts-$BiVO_4$ and ms-$BiVO_4$ have similar band gaps (2.3 eV and 2.4 eV, respectively[11]). The significantly enhanced photocatalytic activity of ms-$BiVO_4$ over ts-$BiVO_4$ could be somehow related to the monoclinic distortion, albeit the underlying mechanism still remains ambiguous. Therefore, in order to better understand the phase-dependent photocatalytic performance, it would be necessary to develop an accurate description of the structural properties of ts-$BiVO_4$ and ms-$BiVO_4$ as well as how the atomic-structure changes affect their electronic structures.

Density functional theory (DFT) is perhaps the most successful computational method for calculation of the structural and electronic properties of semiconductor/oxide materials.[14] DFT is in principle an exact approach to predict ground-state properties; however, in practice the results rely on approximations for the exchange-correlation (xc) potential which accounts for the many-body electron-electron interaction. The xc energy functional is most commonly approximated within the local density approximation (LDA) or generalized gradient approximation (GGA). Despite the great success, the DFT-LDA/GGA approach also causes systematic errors in the electronic structure description; for instance, DFT tends to underestimate by about 30%–40% the band gap of semiconductors and oxides.[15] In addition, standard DFT-LDA/GGA calculations often show their limitations for predicting the properties of strongly correlated materials containing elements with partially filled d or f subshells. This problem is related to the inherent self-interaction error (due to the approximate exchange) of standard DFT, which erroneously favors charge delocalization.[16,17]

In recent years, hybrid DFT methods,[18–20] in which the exact nonlocal Hartree-Fock (HF) exchange is partially mixed with the local or semilocal DFT exchange, have been widely used for the study of solid-state materials. In particular, such hybrid functionals have been found to give a significantly improved description of the structural and electronic properties of metal oxides, such as ZnO, $BaTiO_3$, $SrTiO_3$, and $BiFeO_3$.[21–24] A few DFT studies[1,25–27] have recently been undertaken to examine ms-$BiVO_4$, but they are all based on conventional LDA or GGA xc functionals. As detailed later, we have found that the standard DFT-LDA/GGA approach has a tendency to energetically favor the tetragonal phase (ts-$BiVO_4$) over the monoclinic phase (ms-$BiVO_4$) under ambient pressure and temperature, which is inconsistent with previous experimental observations.[28,29] This implies that standard DFT might be limited in use for accurately describing the lattice distortion and electronic structure of ms-$BiVO_4$.

In this work, we perform both standard DFT and hybrid DFT calculations to explore how the partial inclusion of HF exchange influences the accuracy of predicting the structural,

bonding, and electronic properties of $BiVO_4$. We first calculate the relative thermodynamic stability between ts-$BiVO_4$ and ms-$BiVO_4$ under various strain conditions, together with determination of their lattice parameters and bulk moduli with varying fractions of HF exchange. Based on the results, we discuss the impact of HF exchange inclusion on the description of pressure-induced monoclinic-to-tetragonal phase transition and the prediction accuracy of structural properties. Then, we perform an analysis of Bader charges, charge density differences, and electron density of states to gain a better understanding of the xc functional dependence of the structural stability and properties. Finally, we examine the sensitivity of predicted band structures to the choice of xc functional. This work will help choose an xc functional that can be used to reliably describe the structure-property relationship of $BiVO_4$, which in turn contributes to a better understanding of the function and performance of $BiVO_4$-based materials for various applications, including photocatalysis.

II. CRYSTAL STRUCTURE AND BONDING MECHANISM

In the scheelite-type $BiVO_4$ structure, as illustrated in Fig. 1(a), isolated VO_4 tetrahedra (in gray) are corner connected by BiO_8 dodecahedra (in purple). At ambient conditions, the scheelite-type $BiVO_4$ structure has been found to exhibit a slight monoclinic distortion, while the crystal structure of many other scheelite-type ABO_4 compounds has tetragonal symmetry (space group $I4_1/a$).[30] Earlier experiments[28,29,31] provided evidence that the monoclinic scheelite structure (ms-$BiVO_4$) may undergo transformation to the tetragonal scheelite structure (ts-$BiVO_4$) at about 255 °C or 1.5 GPa. In ts-$BiVO_4$ [Fig. 1(b)], Bi^{3+} and V^{5+} cations are located at the centrosymmetric sites of respective BiO_8 and VO_4 polyhedra, giving four equivalent V-O bonds and two sets of four equivalent Bi-O bonds.[28,31] In ms-$BiVO_4$ [Fig. 1(c)], Bi^{3+} and V^{5+} cations are displaced from the centrosymmetric sites along the c axis (indicated by the
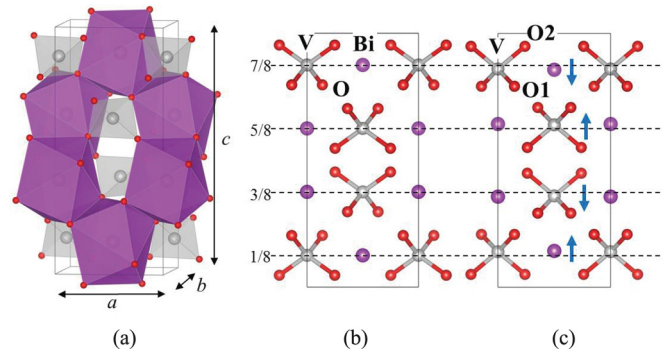

FIG. 1. (Color online) (a) Crystal structure representation of scheelite $BiVO_4$ with indication of BiO_8 dodecahedra (in purple) and VO_4 tetrahedra (in gray), together with (b) ts-$BiVO_4$ and (c) ms-$BiVO_4$ structures projected along the [1 0 0] direction. The arrows [in (c)] represent cation displacements along the c axis with respect to the corresponding positions in ts-$BiVO_4$ (indicated by dotted lines). In ms-$BiVO_4$ [(c)], two different kinds of O atoms are indicated by O1 and O2 (see also Table I). Purple, silver, and red balls represent Bi, V, and O atoms, respectively; Bi-O bonds are omitted for clarity.

arrow), lowering the point symmetry of cation sites from S_4 to C_2.[25,28,31] Table I summarizes the lattice parameters, fractional atomic coordinates, and Bi-O/V-O bond distances as previously measured for ts-$BiVO_4$ and ms-$BiVO_4$.[31]

Recent theoretical studies[1,25,32] have suggested that the energetically favored monoclinic distortion would be associated with hybridization between Bi $6s$, Bi $6p$, and O $2p$ states, as rationalized below. In ts-$BiVO_4$, the coupling between occupied Bi $6s$ and O $2p$ states gives rise to bonding and antibonding states below the Fermi level. The Bi $6s$-O $2p$ antibonding destabilization could be reduced by additional mixing with unoccupied Bi $6p$ states,[32] as illustrated in Fig. 2. Note that the interaction between Bi $6p$ and Bi $6s$ states can only take place in the site with no inversion symmetry,

TABLE I. Experimental crystallographic parameters for ms-$BiVO_4$ (at 4.5 and 295 K) and ts-$BiVO_4$ (at 566 K) from neutron powder diffraction data (Ref. 31). ms-$BiVO_4$ and ts-$BiVO_4$ belong to space groups $I2/b$ and $I4_1/a$, respectively. Measured atomic fractional positions and bond lengths are also listed.

|	Monoclinic		Tetragonal
	4.5 K	295 K	566 K
		Lattice parameter	
a	5.2146	5.1935	5.147
b	5.0842	5.0898	5.147
c	11.7063	11.6972	11.7216
γ	90.39	90.39	
		Atomic position	
Bi	(0, 0.250, 0.636)	(0, 0.250, 0.634)	(0, 0.250, 0.625)
V	(0, 0.250, 0.139)	(0, 0.250, 0.130)	(0, 0.250, 0.125)
O1	(0.151, 0.510, 0.210)	(0.147, 0.508, 0.208)	(0.138, 0.499, 0.203)
O2	(0.263, 0.381, 0.448)	(0.261, 0.381, 0.449)	
		Bond length (Å)	
Bi-O	2.314 × 2, 2.349 × 2	2.354 × 2, 2.372 × 2	2.453 × 4
	2.533 × 2, 2.676 × 2	2.516 × 2, 2.628 × 2	2.499 × 4
V-O	1.74 × 2, 1.75 × 2	1.69 × 2, 1.77 × 2	1.72 × 4
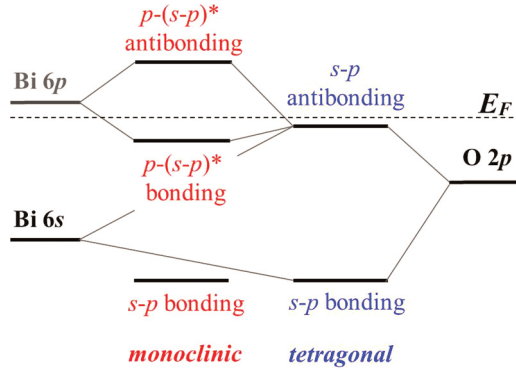
FIG. 2. (Color online) Schematic representation of the interactions between Bi $6s$, Bi $6p$, and O $2p$ orbitals in ts-BiVO$_4$ (in blue) and ms-BiVO$_4$ (in red). The asterisk (*) denotes an antibonding state, and the dashed horizontal line indicates the Fermi level (E_F).

due to symmetry constraints. As such, the Bi $6s$-$6p$ orbital interaction is forbidden in ts-BiVO$_4$, since Bi is located in the centrosymmetric site; hence, the Bi $6s$ lone pair remains spherically symmetric like a pure s-atomic orbital and is stereochemically inactive. On the other hand, the off-centrosymmetric distortion in ms-BiVO$_4$ allows the interaction between Bi $6s$ and Bi $6p$ states, and thus the Bi lone pair is asymmetrically distributed and becomes stereochemically active.[33]

III. COMPUTATIONAL METHODS

The DFT calculations reported herein were performed using the Vienna *ab initio* Simulation Package (VASP 5.2.2).[34] The projector augmented wave (PAW) method with a plane-wave basis set was used to describe the interaction between core and valence electrons.[35] The valence-electron configurations considered are $5d^{10}6s^26p^3$ for Bi, $3p^63d^34s^2$ for V, and $2s^22p^4$ for O. All BiVO$_4$ structures were optimized using a conjugated gradient method until the residual forces on constituent atoms become smaller than 0.01 eV/Å; the cut-off energies for the plane-wave expansion were 750 eV and 550 eV for cell shape/volume and subsequent atomic coordinate optimizations, respectively. The Brillouin zone sampling was performed using a gamma-centered ($4 \times 4 \times 4$) Monkhorst-Pack k-point mesh[36] in geometry optimization, and the k-point mesh size was increased up to ($6 \times 6 \times 6$) to reevaluate the electronic structures.

We employed the Perdew-Burke-Ernzerhof (PBE) xc functional,[37] and replaced a portion of the PBE exchange with exact HF exchange to obtain a hybrid functional. The HF exchange interaction decays slowly with distance, making the conventional hybridization problematic for solids.[38,39] Hence, we employed the Heyd-Scuseria-Ernzerhof (HSE) screened hybrid[40] in which long-range HF is excluded. That is, the exchange term is split into short-range (SR) and long-range (LR) parts, and a fraction of SR HF exchange is only included. As such, the xc energy is given by

$$E_{xc}^{HSE} = \alpha E_x^{HF,SR}(\mu) + (1 - \alpha) E_x^{PBE,SR}(\mu)$$
$$+ E_x^{PBE,LR}(\mu) + E_c^{PBE},$$

where the range-separation parameter μ determines the partition of the SR and LR components. In this work, $\mu = 0.207$ Å^{-1} was used, which has already been demonstrated to be a reasonable compromise between accuracy and computational cost.[39] While still providing reasonable results,[38–40] the screed hybrid approach significantly reduces computation time. In this work, we considered four different xc functionals with $\alpha = 0$, 0.1, 0.25, and 0.5.

IV. RESULTS AND DISCUSSION

A. Relative phase stability and lattice parameters: Tetragonal vs monoclinic

We first looked at the relative thermodynamic stability between ts-BiVO$_4$ and ms-BiVO$_4$ as a function of unit-cell volume for different xc functionals. From a thermodynamic point of view, the relative stability between two systems can be determined by their Gibbs free energy difference ($\Delta G = \Delta E + P\Delta V - T\Delta S$); for a given volume (i.e., $\Delta V = 0$), we simplified the calculations by only considering the difference of internal energy (ΔE) at 0 K.

Figure 3 shows calculated energy-volume (E-V) curves for PBE [(a)] and PBE-HF hybrid functionals with different fractions of exact HF exchange [(b) HF10%, (c) HF25%, (d) HF50%]. For each volume, starting with the experimental atomic coordinates (as listed in Table I), the cell shapes and fractional coordinates of ts-BiVO$_4$ and ms-BiVO$_4$ were allowed to relax under the fixed volume constraint. Above the crossover volume (V_C), there is a continuous second-order transformation from ts-BiVO$_4$ to ms-BiVO$_4$ with increasing volume. Given the inverse relationship between pressure and volume, our calculation result clearly demonstrates the occurrence of monoclinic-to-tetragonal phase transition with pressure increase (or volume decrease); this is consistent with the experimental evidence for the pressure-induced second-order phase transition from ms-BiVO$_4$ to ts-BiVO$_4$.[29]
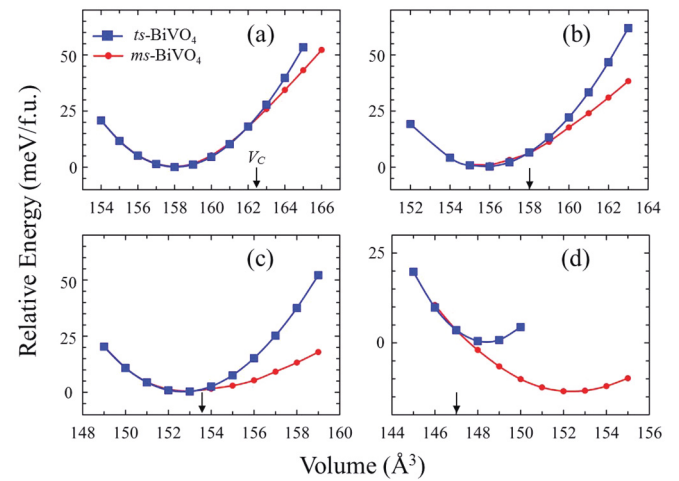

FIG. 3. (Color online) Relative energies per formula unit (f.u.) for ts-BiVO$_4$ and ms-BiVO$_4$ with respect to the lowest energy structure of ts-BiVO$_4$ as a function of volume calculated using (a) pure PBE, (b) PBE-HF10%, (c) PBE-HF25%, and (d) PBE-HF50%. For each case, the crossover volume (V_C) where the energy-volume curves of ts-BiVO$_4$ and ms-BiVO$_4$ meet is indicated by the arrow.

TABLE II. Optimized lattice parameters for ts-BiVO$_4$ and ms-BiVO$_4$ with different xc functionals as specified, together with Bi-O/V-O bond lengths, equilibrium volumes (V_0), and bulk moduli (B_0).

		Tetragonal			
		PBE	HF 10%	HF 25%	HF 50%
Lattice constant	a	5.178	5.155	5.121	5.076
	c	11.784	11.724	11.647	11.521
Bond length (Å)	Bi-O	2.454 × 4	2.444 × 4	2.431 × 4	2.414 × 4
		2.507 × 4	2.496 × 4	2.481 × 4	2.456 × 4
	V-O	1.746 × 4	1.735 × 4	1.721 × 4	1.701 × 4
V_0 (Å^3)		158.0	155.8	152.7	148.4
B_0 (GPa)		122.1	128.5	138.2	156.4
		Monoclinic			
		HF 25%		HF 50%	
Lattice constant	a/b	5.183/5.074		5.197/5.006	
	c	11.711		11.722	
	γ	90.36		90.81	
Bond length (Å)	Bi-O	2.378 × 2, 2.384 × 2		2.283 × 2, 2.335 × 2	
		2.485 × 2, 2.619 × 2		2.527 × 2, 2.729 × 2	
	V-O	1.693 × 2, 1.751 × 2		1.651 × 2, 1.758 × 2	
V_0 (Å^3)		154.0		152.5	
B_0 (GPa)				56.3	

While the phase transition behavior is generally consistent with previous experimental observations, it is interesting to note the sensitivity of V_C to the HF exchange weight. The relative crossover volume (V_C^*) respective to the equilibrium volume of ts-BiVO$_4$ (V_0^t), given by $V_C^* = (V_C - V_0^t)/V_0^t$, decreases from 0.028, 0.014, 0.005 to -0.009 with increasing the fraction of HF exchange from 0% (equivalent to PBE), 10%, 25% to 50%, respectively. Here, V_0^t is obtained by fitting a set of the E-V data to the third-order Birch-Murnaghan equation of state.[41] Recall that the ms-BiVO$_4 \rightarrow ts$-BiVO$_4$ transition may occur under compressive stress conditions (≈ 1.5 GPa), according to earlier experiment.[29] To comply with this, V_C^* needs to be negative, which suggests that hybrid functionals with a sizable fraction of HF exchange would be required to properly evaluate the relative stability between ts-BiVO$_4$ and ms-BiVO$_4$.

In Table II, we summarized calculated lattice factors (a, b, c, and γ), bulk moduli (B_0), and equilibrium volumes (V_0) for the optimized ts-BiVO$_4$ and ms-BiVO$_4$ structures with different HF exchange fractions. For ms-BiVO$_4$, only PBE-HF25% and PBE-HF50% results are reported because PBE and PBE-HF10% are not sufficient to yield the respective equilibrium configurations; instead ms-BiVO$_4$ tends to merge to ts-BiVO$_4$ (see Fig. 3). With increasing the HF exchange weight, the monoclinic angle (γ) increases; the predicted γ of 90.36° with PBE-HF25% is close to the experimental value of 90.39°, whereas PBE-HF50% ($\gamma = 90.81°$) tends to overestimate the lattice distortions. Concomitantly, the difference between a and b increases with HF exchange fraction; note that the monoclinic distortion is associated with the displacement of Bi from the centrosymmetric site, yielding $a \neq b$ and $\gamma > 90°$ (while $a = b$ and $\gamma = 90°$ in ts-BiVO$_4$).

In comparison, previous conventional DFT calculations[26,27] yielded $\gamma \approx 90°$ and $a \approx b$ for ms-BiVO$_4$, which is consistent with our calculations (from which the ms-BiVO$_4$ structure nearly merges to the ts-BiVO$_4$ structure upon structural

relaxation with PBE, as also pointed out earlier). Furthermore, predicted Bi-O and V-O bond distances with PBE-HF25% are very close to the experimental values (see Table I). Our calculations also predict the B_0 of ts-BiVO$_4$ to be greater than that of ms-BiVO$_4$, consistent with existing experimental measurements ($B_0 = 145$ GPa for ts-BiVO$_4$ is greater than 65 GPa for ms-BiVO$_4$).[29] In addition, overall B_0 increases, while V_0 decreases with increasing the amount of HF exchange.

B. Electronic structure description: Standard vs hybrid DFT

To gain a better understanding of the xc functional dependence of the structural stability, we investigated how the inclusion of HF exchange affects the description of bonding in ts-BiVO$_4$ and ms-BiVO$_4$. In Fig. 4, the isosurface plots show the differences between the charge densities calculated using PBE-HF50% and PBE (based on the BiVO$_4$ configurations optimized with PBE-HF50%, i.e., $\Delta\rho = \rho^{HF50} - \rho^{PBE}$) for (a) ts-BiVO$_4$ and (b) ms-BiVO$_4$. Here, HF50% was chosen, rather than HF10% or 25%, to demonstrate more clearly the HF exchange contribution. The yellow and blue isosurfaces represent charge gain ($\Delta\rho > 0$) and charge loss ($\Delta\rho < 0$), respectively.

For both ts-BiVO$_4$ and ms-BiVO$_4$, the $\Delta\rho$ plots clearly demonstrate that the charge gain of O anions is enhanced, while the charge on Bi and V cations is more depleted upon the inclusion of HF exchange. It is worthwhile to note the asymmetric isosurface around Bi in ms-BiVO$_4$, which is due to the charge loss from the asymmetric Bi 6s lone pair; on the other hand, the symmetric isosurface in ts-BiVO$_4$ indicates that the Bi 6s lone pair remains spherically symmetric. The increased charge transfer between the cations and anions is expected to increase the ionicity of BiVO$_4$. According to the grid-based Bader analysis[42] we performed (see Table III), in ts-BiVO$_4$ the O charge state is predicted to change from -1.04 (in PBE) to -1.17 (in PBE-HF50%),
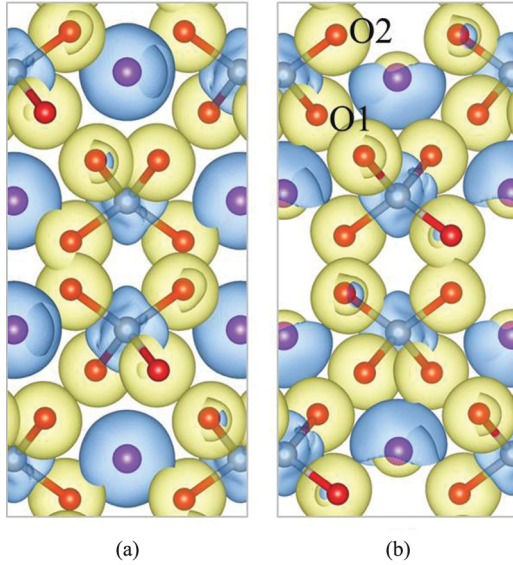
FIG. 4. (Color online) Charge density differences between PBE and PBE-HF50% results ($\Delta\rho = \rho^{\text{HF50}} - \rho^{\text{PBE}}$) for (a) ts-BiVO$_4$ and (b) ms-BiVO$_4$. Yellow ($\Delta\rho > 0$) and blue ($\Delta\rho < 0$) isosurfaces respectively correspond to an excess ($+0.022\ e/\text{Å}^3$) and deficiency ($-0.022\ e/\text{Å}^3$) of electronic charge. Purple, silver, and red balls represent Bi, V, and O atoms, respectively; all Bi-O bonds are omitted for clarity.

while Bi/V cations become more positively charged ($+2.05/2.11 \rightarrow +2.27/2.42$); a similar result is obtained for ms-BiVO$_4$. The Bader volume is also found to increase (or decrease) as the charge gain (or loss) is enhanced, following the general trend that ionic radius increases (or decreases) with increasing negative (or positive) charge, as also demonstrated by previous studies.[24]

Figure 5 shows the electron density of states (DOS) projected onto the $6s$ and $6p$ orbitals of Bi in ts-BiVO$_4$ from PBE [(a)], PBE-HF25% [(b)], and PBE-HF50% [(c)] calculations. This DOS analysis clearly shows that the interaction between the filled Bi $6s$ and O $2p$ states gives rise to bonding and antibonding states; the bonding states (8–11 eV below the Fermi level) are dominated by Bi $6s$ states with minor contributions from O $2p$ states, while the antibonding states (near the top of the valence band) are composed mainly of O $2p$ states with minor Bi $6s$ states (insets in Fig. 5). This is consistent with previous DFT calculations.[1,25]

As the HF exchange weight is increased, the Bi $6s$ contribution to the top of the valence band becomes more pronounced, indicating a stronger antibonding interaction between Bi $6s$
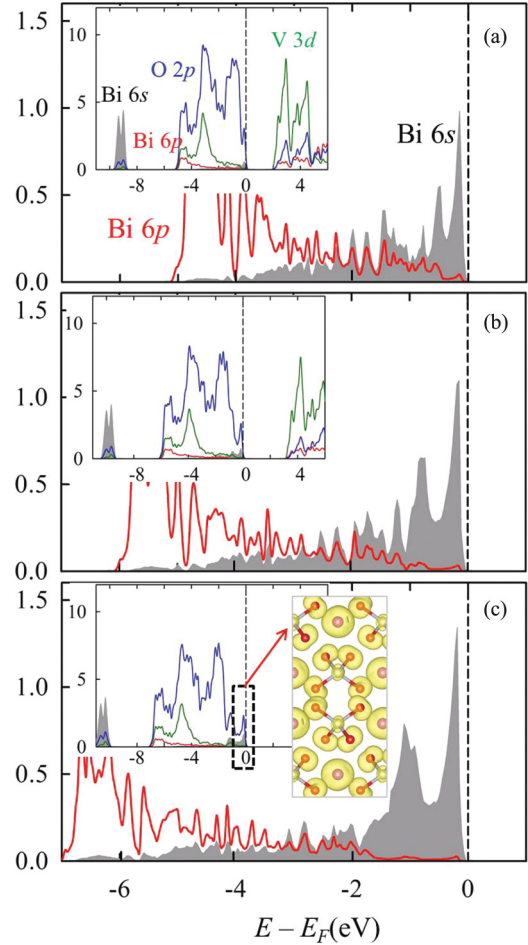

FIG. 5. (Color online) Electron DOS projected onto Bi $6s$ (shaded in gray) and Bi $6p$ (red solid line) states in ts-BiVO$_4$ calculated using (a) pure PBE, (b) PBE-HF25%, and (c) PBE-HF50%. In the insets, the blue and green solid lines indicate O $2p$ and V $3d$ states, respectively. The energy zero is set at the Fermi level (E_F), which is indicated by the vertical dashed lines. The inset of (c) shows the band-decomposed charge density (within $-1.40\ \text{eV} < E - E_F < 0\ \text{eV}$, as indicated by the dashed box, with an isosurface value of $0.06\ e/\text{Å}^3$) from PBE-HF50% calculations; purple, silver, and red balls represent Bi, V, and O atoms, respectively.

and O $2p$ states. Note that, in the (high-symmetry) tetragonal phase, there is no noticeable secondary coupling of Bi $6s$ and $6p$ states near the valence-band top, due to the orbital symmetry constraint as also evidenced by the spherically symmetric (s-like) charge distribution of Bi ions [see inset of Fig. 5(c)]. In addition, we can see that the increase of the

TABLE III. Bader charges of Bi, V, and O atoms in ts-BiVO$_4$ and ms-BiVO$_4$ from PBE-HF50% calculations; the values in parentheses are from pure PBE calculations using the same geometries as obtained with PBE-HF50%.

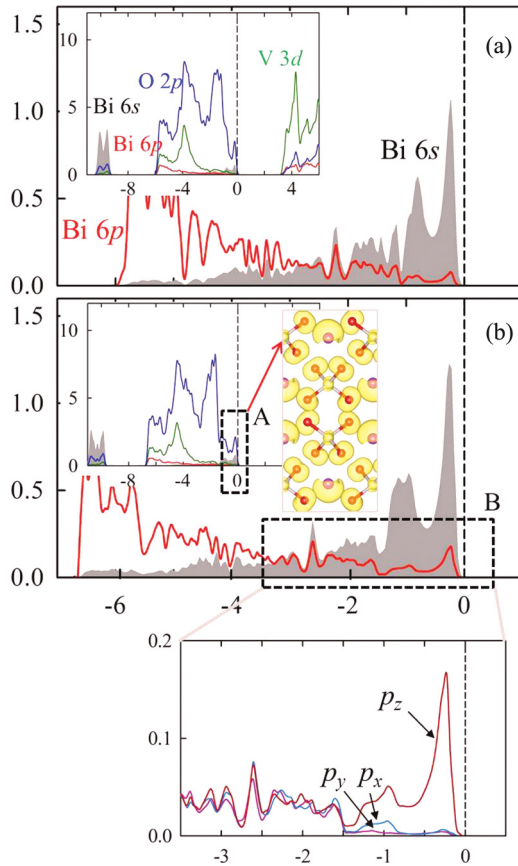| Tetragonal			
Bi	V	O	
$+2.27\ (+2.05)$	$+2.42\ (+2.11)$	$-1.17\ (-1.04)$	
Monoclinic			
Bi	V	O1	O2
$+2.25\ (+2.04)$	$+2.41\ (+2.11)$	$-1.24\ (-1.10)$	$-1.09\ (-0.97)$

FIG. 6. (Color online) Electron DOS projected onto Bi $6s$ (shaded in gray) and Bi $6p$ (red solid line) states in ms-BiVO$_4$ calculated using (a) PBE-HF25% and (b) PBE-HF50%. In the insets, the blue and green solid lines indicate O $2p$ and V $3d$ states, respectively. The energy zero is set at the Fermi level (E_F), which is indicated by the vertical dashed lines. The inset A of (b) shows the band-decomposed charge density (within -1.40 eV $< E - E_F < 0$ eV, as indicated by the dashed box, with an isosurface value of 0.06 $e/$Å^3) from PBE-HF50% calculations; purple, silver, and red balls represent Bi, V, and O atoms, respectively. The projected DOS for Bi $6p_x$ (cyan), $6p_y$ (purple), and $6p_z$ (brown) states are also shown below (b).

HF exchange portion leads to a broadening and downshift of the valence band while increasing the band gap, which is a well-known feature of hybrid DFT methods; recall that pure HF tends to overestimate band widths and band gaps.[24]

Figure 6 shows the ion-projected valence-electron DOS for ms-BiVO$_4$; only PBE-HF25% [(a)] and PBE-HF50% [(b)] cases were considered as no minimum-energy monoclinic structure was obtained within pure PBE/PBE-HF10%. Overall, the DOS features are similar to those for ts-BiVO$_4$, except the appearance of Bi $6p$ states at the valence-band top (while their intensity is more pronounced with HF exchange weight). This supports the hybridization between Bi $6s$-O $2p$ antibonding states and unoccupied Bi $6p$ states in ms-BiVO$_4$ (where the Bi site no longer has inversion symmetry due to its off-center displacement, as mentioned earlier). That is, the symmetry-lowering distortion stabilizes the occupied antibonding states near the Fermi level by allowing them to mix with the empty conduction-band states at the expense of increased strain energy.[1,25,32] As shown in the inset B of
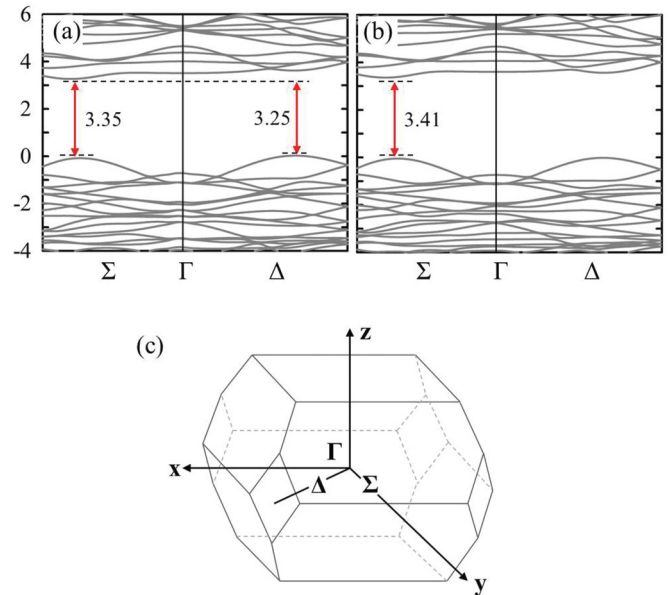

FIG. 7. (Color online) Band structure diagrams for (a) ts-BiVO$_4$ and (b) ms-BiVO$_4$ from PBE-HF25% calculations, together with (c) Brillouin zone for a body-centered tetragonal crystal structure. The bands are plotted along Σ and Δ directions as specified in (c); for each case, the energy zero is set at the top of the valence band. The direct/indirect band-gap values are also indicated.

Fig. 6(b), the analysis of decomposed Bi $6p_x$, $6p_y$, $6p_z$, and $6s$ orbitals demonstrates that only the p_z orbitals effectively overlap with the s orbitals. This can be explained by the fact that the s orbitals are asymmetrically distributed with lone-pair lobes aligned in the z direction (note that orbitals are allowed to interact with each other if they have compatible symmetries, according to the molecular orbital theory). This analysis reveals that the antibonding interaction between filled Bi $6s$ and O $2p$ orbitals increases with increasing the amount of HF exchange. Therefore, the energy gain from the additional mixing with unoccupied Bi $6p$ states concomitantly increases to exceed the strain energy caused by the monoclinic distortion; this leads the monoclinic phase to be more energetically favorable the tetragonal phase when the HF exchange fraction is greater than 25% (see Fig. 3).

Figure 7 shows band structure diagrams calculated for ts-BiVO$_4$ [(a)] and ms-BiVO$_4$ [(b)] optimized within PBE-HF25%, along two high-symmetry directions (Σ and Δ) (or equivalent directions for ms-BiVO$_4$) in the Brillouin zone[43,44] [(c)]. We also calculated the band structures for PBE/PBE-HF50%-optimized ts-BiVO$_4$ and PBE-HF50%-optimized ms-BiVO$_4$. Overall, the band shapes turn out to be insignificantly affected by the xc functional choice, while the band gaps increase considerably with increasing the HF exchange fraction (see Table IV).

For ts-BiVO$_4$ [Fig. 7(a)], the valence band has a maximum (VBM) in the Δ direction (which is only about 0.1 eV higher than that in the Σ direction). The conduction-band minimum (CBM) is located midway along the Σ line. The results suggest that the minimum direct gap may lie in the Σ direction, and is slightly higher in energy than the lowest indirect gap. Similar band characteristics have also been reported for tetragonal

TABLE IV. Calculated band gaps for ts-BiVO$_4$ and ms-BiVO$_4$ with PBE-HF25% and PBE-HF50% as specified. The directions along which the VBM and CBM occur are also indicated.

	HF25%			HF50%		
	E_{gap} (eV)	VB	CB	E_{gap} (eV)	VB	CB
ts-BiVO$_4$	3.26	Δ	Σ	4.57	Δ	Σ
	3.35	Σ	Σ	4.68	Σ	Σ
ms-BiVO$_4$	3.41	Σ	Σ	4.99	Σ	Σ

scheelite-type PbWO$_4$ and PbMoO$_4$.[44] As listed in Table IV, the PBE values of 2.12/2.16 eV (indirect/direct) are found to be underestimated, but only marginally, in comparison to the experimental value of 2.34 eV.[11] The predicted indirect/direct gap values increase to 3.26/3.35 eV and 4.57/4.68 eV, respectively, as the fraction of HF exchange increases to 25% and 50%.

For ms-BiVO$_4$ [Fig. 7(b)], the valance-band extrema in the Σ and Δ direction appear (nearly) degenerate, while the CBM lies along the Σ direction, implying that the minimum direct band gap lies in the Σ direction. As summarized in Table IV, the predicted direct gap values of 3.41 eV (PBE-HF25%) and 4.99 eV (PBE-HF50%) for ms-BiVO$_4$ are consistently larger than corresponding 3.26/3.35eV and 4.57/4.68eV for ts-BiVO$_4$; this is consistent with previous experiments [i.e., 2.41–2.5 eV (ms-BiVO$_4$) vs 2.34 eV (ts-BiVO$_4$).[9,11] The band-gap widening in ms-BiVO$_4$ can be attributed mainly to stabilization of the valence-band top (or lowering of the VBM energy) through the coupling of Bi 6s-O 2p antibonding states with Bi 6p states, as discussed earlier. The phase transition is likely to negligibly affect the CBM (dominated by V 3d states with minor contributions from O 2p and Bi 6p). It is also interesting to note that the gap difference between ts-BiVO$_4$ and ms-BiVO$_4$ increases with the extent of HF contribution; this is apparently due to the fact that the increased HF weight enhances the mixing of Bi 6s and 6p states and thus lowers the VBM in energy.

V. SUMMARY

We calculated the structural, bonding, and electronic properties of two important phases of BiVO$_4$, tetragonal scheelite (ts-BiVO$_4$) and monoclinic scheelite (ms-BiVO$_4$), within DFT using the PBE and the PBE-HF hybrid functionals with varying HF exchange fractions (10%, 25%, and 50%). Based on the results, we attempted to examine how the inclusion of exact HF exchange improves the accuracy of predicting the properties of BiVO$_4$. We find that the PBE and PBE-HF10%

calculations would fail to identify the stable structure of ms-BiVO$_4$ under strain-free conditions; they also predict the occurrence of monoclinic-to-tetragonal phase transition only under tensile strain, in contradiction with experiment. Among the applied functionals, the PBE-HF25% predicts a monoclinic configuration very close to the experimentally observed structure, while the PBE-HF50% tends to noticeably overestimate the monoclinic distortion. Density of states analysis reveals that an increase in the amount of HF exchange leads to enhancement of the antibonding interaction between Bi 6s and O 2p states; as a consequence, hybridization between Bi 6s-O 2p antibonding states and unoccupied Bi 6p states becomes more pronounced to reduce the antibonding interaction through the monoclinic lattice distortion. This suggests that the resulting energy gain exceeding the strain energy (caused by the monoclinic distortion) is primarily responsible for prediction of energetically favored ms-BiVO$_4$ over ts-BiVO$_4$ when the HF exchange fraction is greater than 25%. In addition, analysis of Bader charges and charge density differences clearly demonstrates an increase in the charge transfer between Bi/V cations and O anions in both ts-BiVO$_4$ and ms-BiVO$_4$ as the amount of HF exchange increases. We finally calculated the band structures of ts-BiVO$_4$ and ms-BiVO$_4$; overall the results show that the shapes of the bands are insignificantly affected by the xc functional choice, but the band gaps increase considerably with increasing the HF exchange fraction. ms-BiVO$_4$ and ts-BiVO$_4$ are predicted to have direct and indirect band gaps, respectively, while the former is slightly larger than the latter; the band-gap widening in ms-BiVO$_4$ can be largely attributed to stabilization of the valence-band top through the coupling of Bi 6s-O 2p antibonding states with Bi 6p states. Our work clearly demonstrates that the inclusion of HF exchange has a positive impact on the overall prediction accuracy for the structural and electronic properties of BiVO$_4$, while also providing some guidelines for choosing a hybrid xc functional that can perform well for a specific application. Moreover, the improved understanding of the structure-property relationship attained from this work will greatly assist in uncovering many puzzling questions related to the function and performance of BiVO$_4$-based materials for various applications, such as its strong phase-dependent photocatalytic activity.

*Author to whom correspondence should be addressed: gshwang@che.utexas.edu

[1]A. Walsh, Y. Yan, M. N. Huda, M. M. Al-Jassim, and S. Wei, Chem. Mater. **21**, 547 (2009).

[2]R. van de Krol and M. Grätzel, *Photoelectrochemical Hydrogen Production*, Electronic Materials: Science & Technology Vol. 102 (Springer, New York, 2012).

[3]L. Zang, *Energy Efficiency and Renewable Energy through Nanotechnology*, Green Energy and Technology (Springer-Verlag, London, 2011).

[4]M. D. Hernández-Alonso, F. Fresno, S. Suárez, and J. M. Coronado, Energy Environ. Sci. **2**, 1231 (2009).

[5]X. Wang, J. C. Yu, C. Ho, Y. Hou, and X. Fu, Langmuir **21**, 2552 (2005).

[6] A. Kudo, K. Omori, and H. Kato, J. Am. Chem. Soc. **121**, 11459 (1999).

[7] H. Luo, A. H. Mueller, T. M. McCleskey, A. K. Burrell, E. Bauer, and Q. X. Jia, J. Phys. Chem. C **112**, 6099 (2008).

[8] K. Sayama, A. Nomura, T. Arai, T. Sugita, R. Abe, M. Yanagida, T. Oi, Y. Iwasaki, Y. Abe, and H. Sugihara, J. Phys. Chem. B **110**, 11352 (2006).

[9] H. S. Park, K. E. Kweon, H. Ye, E. Paek, G. S. Hwang, and A. J. Bard, J. Phys. Chem. C **115**, 17870 (2011).

[10] H. Ye, J. Lee, J. S. Jang, and A. J. Bard, J. Phys. Chem. C **114**, 13322 (2010).

[11] S. Tokunaga, H. Kato, and A. Kudo, Chem. Mater. **13**, 4624 (2001).

[12] J. Yu and A. Kudo, Adv. Funct. Mater. **16**, 2163 (2006).

[13] J. D. Bierlein and A. W. Sleight, Solid State Commun. **16**, 69 (1975).

[14] *Computational Photochemistry*, edited by M. Olivucci, Theoretical and Computational Chemistry Vol. 16 (Elsevier, Amsterdam, 2005), pp. 93–128.

[15] A. Alkauskas, P. Deák, J. Neugebauer, A. Pasquarello, and C. G. Van de Walle, *Advanced Calculations for Defects in Materials* (Wiley-VCH, Weinheim, 2011).

[16] P. Mori-Sánchez, A. J. Cohen, and W. Yang, Phys. Rev. Lett. **100**, 146401 (2008).

[17] A. J. Cohen, P. Mori-Sánchez, and W. Yang, Science **321**, 792 (2008).

[18] A. D. Becke, J. Chem. Phys. **98**, 1372 (1993).

[19] A. D. Becke, J. Chem. Phys. **98**, 5648 (1993).

[20] C. Adamo and V. Barone, Chem. Phys. Lett. **274**, 242 (1997).

[21] J. Wróbel, K. J. Kurzydłowski, K. Hummer, G. Kresse, and Jacek Piechota, Phys. Rev. B **80**, 155124 (2009).

[22] D. I. Bilc, R. Orlando, R. Shaltaf, G. M. Rignanese, J. Iniguez, and P. Ghosez, Phys. Rev. B **77**, 165107 (2008).

[23] R. Wahl, D. Vogtenhuber, and G. Kresse, Phys. Rev. B **78**, 104116 (2008).

[24] A. Stroppa and S. Picozzi, Phys. Chem. Chem. Phys. **12**, 5405 (2010).

[25] M. W. Stoltzfus, P. M. Woodward, R. Seshadri, J.-H. Klepeis, and B. Bursten, Inorg. Chem. **46**, 3839 (2007).

[26] W. J. Yin, S. H. Wei, M. M. Al-Jassim, J. Turner, and Y. Yan, Phys. Rev. B **83**, 155102 (2011).

[27] Z. Zhao, Z. Li, and Z. Zou, Phys. Chem. Chem. Phys. **13**, 4746 (2011).

[28] W. I. F. David and I. G. Wood, J. Phys. C **16**, 5127(1983).

[29] R. M. Hazen and J. W. E. Mariathasan, Science **216**, 991 (1982).

[30] D. Errandonea and F. J. Manjón, Prog. Mater. Sci. **53**, 711 (2008).

[31] A. W. Sleight, H.-Y. Chen, and A. Ferretti, Mater. Res. Bull. **14**, 1571 (1979).

[32] A. Walsh, D. J. Payne, R. G. Egdell, and G. W. Watson, Chem. Soc. Rev. **40**, 4455 (2011).

[33] Ralph A. Wheeler and P. N. V. Pavan Kumar, J. Am. Chem. Soc. **114**, 4776 (1992).

[34] G. Kresse and J. Furthmuller, *VASP: The Guide* (Vienna University of Technology, Vienna, Austria, 2001).

[35] P. E. Blöchl, Phys. Rev. B **50**, 17953 (1994).

[36] H. J. Monkhorst and J. D. Pack, Phys. Rev. B **13**, 5188 (1976).

[37] J. P. Perdew, K. Burke, and M. Ernzerhof, Phys. Rev. Lett. **77**, 3865 (1996).

[38] J. Paier, M. Marsman, K. Hummer, G. Kresse, I. C. Gerber, and J. G. Ángyán, J. Chem. Phys. **124**, 154709 (2006).

[39] L. Schimka, J. Harl, and G. Kresse, J. Chem. Phys. **134**, 024116 (2011).

[40] J. Heyd, G. E. Scuseria, and M. Ernzerhof, J. Chem. Phys. **118**, 8207 (2003).

[41] F. Birch, J. Geophys. Res. **83**, 1257 (1978).

[42] G. Henkelman, A. Arnaldsson, and H. Jónsson, Comput. Mater. Sci. **36**, 354 (2006).

[43] H. Yamagami and A. Hasegawa, J. Phys. Soc. Jpn. **61**, 2388 (1992).

[44] Y. Zhang, N. A. W. Holzwarth, and R. T. Williams, Phys. Rev. B **57**, 12738 (1998).